

# Spatial scale evaluation of forecast flood inundation maps

Helen Hooker<sup>1</sup>, h.hooker@pgr.reading.ac.uk

Sarah L.Dance<sup>1,2,3</sup>, s.l.dance@reading.ac.uk

David C.Mason<sup>4</sup>, d.c.mason@reading.ac.uk

John Bevington<sup>5</sup>, john.bevington@jbaconsulting.com

Kay Shelton<sup>5</sup>, kay.shelton@jbaconsulting.com

<sup>1</sup>Department of Meteorology, University of Reading, UK

<sup>2</sup>Department of Mathematics and Statistics, University of Reading, UK

<sup>3</sup>National Centre for Earth Observation (NCEO), Reading, UK

<sup>4</sup>Department of Geography and Environmental Science, University of Reading, UK

<sup>5</sup>Jeremy Benn Associates Limited (JBA Consulting), UK

This paper is a non-peer reviewed preprint submitted to EarthArXiv. A preprint has been submitted to the Journal of Hydrology for publication.

## Highlights

### **Spatial scale evaluation of forecast flood inundation maps**

Helen Hooker, Sarah L. Dance, David C. Mason, John Bevington, Kay Shelton

- A novel spatial scale-selective approach to evaluate forecast flood maps against Synthetic Aperture Radar data.
- Validation of the flood edge gives a physically meaningful measure of prediction accuracy.
- Conventional contingency flood maps are improved by including a location specific skilful spatial scale.

# Spatial scale evaluation of forecast flood inundation maps

Helen Hooker<sup>a</sup>, Sarah L. Dance<sup>a,b,d</sup>, David C. Mason<sup>c</sup>, John Bevington<sup>e</sup>,  
Kay Shelton<sup>e</sup>

<sup>a</sup>*Department of Meteorology, University of Reading, UK*

<sup>b</sup>*Department of Mathematics and Statistics, University of Reading, UK*

<sup>c</sup>*Department of Geography and Environmental Science, University of Reading, UK*

<sup>d</sup>*National Centre for Earth Observation (NCEO), University of Reading, UK*

<sup>e</sup>*Jeremy Benn Associates Limited (JBA Consulting), Skipton, UK*

---

## Abstract

Flood inundation forecast maps provide an essential tool to disaster management teams for planning and preparation ahead of a flood event in order to mitigate the impacts of flooding on the community. Evaluating the accuracy of forecast flood maps is essential for model development and improving future flood predictions. Conventional, quantitative binary verification measures typically provide a domain averaged score, at grid level, of forecast skill. This score is dependent on the magnitude of the flood and the spatial scale of the flood map. Binary scores have limited physical meaning and do not indicate location specific variations in forecast skill that enable targeted model improvements to be made. A new, scale-selective approach is presented here to evaluate forecast flood inundation maps against remotely observed flood extents. A neighbourhood approach based on the Fraction Skill Score is applied to assess the spatial scale at which the forecast becomes skilful at capturing the observed flood. This skilful scale varies with location and when combined with a contingency map creates a novel categorical

scale map, a valuable visual tool for model evaluation and development. The impact of model improvements on forecast flood map accuracy skill scores are often masked by large areas of correctly predicted flooded/unflooded cells. To address this, the accuracy of the flood-edge location is evaluated. The flood-edge location accuracy proves to be more sensitive to variations in forecast skill and spatial scale compared to the accuracy of the entire flood extent. Additionally, the resulting skilful scale of the flood-edge provides a physically meaningful verification measure of the forecast flood-edge discrepancy. Representation errors are introduced where remote sensing observations capture flood extent at different spatial resolutions in comparison with the model. Relative to the spatial scale of the forecast flood maps, the errors introduced in high resolution observations can cause the observed flood extent to be over-estimated with lower resolution observations leading to under-estimation. This has implications for future studies where observations are taken from multiple heterogeneous sources. Overall, our novel emphasis on scale, rather than domain-average score, means that comparisons can be made across different flooding scenarios and forecast systems and between forecasts at different spatial scales.

*Keywords:* Flood maps, Spatial verification, Scale selective, SAR

---

## 1. Introduction

Timely predictions of flood extent and depth from flood forecasting systems provide essential information to flood risk managers that enable anticipatory action prior to the occurrence of a potential flooding event. Evaluating the accuracy of flood extent forecasts against observations forms an essential

6 part of model development. Forecast flood inundation footprints are typically  
7 validated against remote sensing images using binary performance measures  
8 (Stephens et al., 2014) calculated at grid level. In order to produce a forecast  
9 flood map, hydrodynamic or hydraulic flood models in two-dimensions simu-  
10 late the flow of water using a local digital terrain model (DTM). The spatial  
11 resolution of DTMs has increased over recent years and is important for ac-  
12 curate flood mapping. For example, in the UK, the Environment Agency  
13 National LIDAR Programme offers open source 1 m surface elevation data  
14 for the whole of England (Environment Agency, 2021). Additional surface  
15 detail to 0.3 m spatial resolution from unmanned aerial vehicle UAV-LIDAR  
16 data acquired in urban areas is now possible (Trepekli et al., 2021). This  
17 means forecast flood maps could be presented at this very high resolution. It  
18 is questionable how meaningful it is to present highly detailed flood maps as  
19 a deterministic forecast. Speight et al. (2021) note for surface water flooding  
20 that more detail is included in local scale flood maps than can be justified by  
21 the predictability of the forecast. A high resolution (HR), fine scale forecast  
22 flood map will show greater detail of the flood extent and the flood-edge  
23 location compared to a low resolution (LR), coarse scale flood map. At HR  
24 the discrepancy between the forecast and observed flood maps may be closer  
25 in terms of distance, however a small mismatch will lead to a double penalty  
26 impact on forecast verification. The model is penalised twice for the over-  
27 prediction (false alarm) and the under-prediction (miss) (Stein and Stoop,  
28 2019). When HR forecasts are verified against observations at grid level, the  
29 predictability can appear to worsen and the HR forecast would need to per-  
30 form better than the LR forecast to achieve the same verification score. It

31 is not meaningful to compare verification scores across different spatial scales.

32

33 Verification approaches that account for uncertainties in observations and  
34 small discrepancies in gridded data using a fuzzy set approach (Hagen, 2003)  
35 have previously been applied to flood mapping (Pappenberger et al., 2007).  
36 However, the fuzzy set method does not incorporate variations in spatial  
37 scale (Cloke and Pappenberger, 2008). In atmospheric sciences, verification  
38 approaches that account for changes in spatial scale are well established.  
39 These approaches include the Fraction Skill Score (FSS), which applies a  
40 neighbourhood approach to assess a useful/skilful scale (Roberts and Lean,  
41 2008) of a precipitation forecast. Dey et al. (2014, 2016) developed the FSS  
42 approach to produce location specific agreement scales between the forecast  
43 and observed fields to understand the spatial predictability of an ensemble  
44 forecast. Other spatial scale approaches include the wavelet method of scale  
45 decomposition, where the forecast and observed fields are decomposed into  
46 maps at different scales by wavelet transformation and subsequently verified  
47 (Briggs and Levine, 1997; Casati and Wilson, 2007). Cloke and Pappen-  
48 berger (2008) note that this method is extremely sensitive to offsetting of  
49 maps. In general, the performance of forecast flood maps are evaluated for  
50 the entire flood extent, regardless of flood magnitude, adding bias to binary  
51 performance measures (Stephens et al., 2014). Stephens et al. (2014) question  
52 whether it is important to validate all flooded cells, when only cells that are  
53 close to the flood margin are difficult to predict. Pappenberger et al. (2007)  
54 evaluated model performance only on cells that were subject to change be-  
55 tween differing model runs to address the issue of large areas of correctly

56 predicted flooded/unflooded cells masking variations in forecast skill scores.

57

58 Satellite based Synthetic Aperture Radar (SAR) sensors are well known  
59 for their flood detection capability. Unobstructed flood waters appear dark  
60 on raw SAR images due to the low backscatter return from the relatively  
61 smooth water surface. SAR sensors also have an advantage over optical in-  
62 struments as they can scan at night and are not impacted by cloud and  
63 weather, usually associated with a flooding situation. In recent years due  
64 to improvements in spatial resolution and more frequent revisit times, SAR  
65 data has been used successfully to calibrate and validate hydrodynamic and  
66 hydraulic forecast models (Schumann et al., 2009; Grimaldi et al., 2016).  
67 Further model improvements have been shown through the assimilation of  
68 SAR data (e.g. García-Pintado et al., 2015; Hostache et al., 2018; Cooper  
69 et al., 2019; Di Mauro et al., 2020; Dasgupta et al., 2018, 2021a,b). Recent  
70 techniques have improved the flood detection in urban areas using medium  
71 and high resolution SAR (Mason et al., 2018, 2021a,b). The Copernicus  
72 Emergency Management Service (CEMS) (Copernicus Programme, 2021) of-  
73 fers freely available, open access Sentinel-1 SAR data. With two satellites  
74 in orbit, 10 m ground resolution and three day revisit times (for the mid-  
75 latitudes), Sentinel-1 data offers good coverage of a potential flood event. For  
76 a major flood event CEMS can be triggered to offer additional rapid flood  
77 mapping. From 2021, the new Global Flood Monitoring (GFM) product  
78 (GFM, 2021; Hostache et al., 2021) of the Copernicus Emergency Manage-  
79 ment Service (CEMS) (Copernicus Programme, 2021) produces Sentinel-1  
80 SAR-derived flood inundation maps using three flood detection algorithms

81 providing uncertainty estimation and population affected estimates within 8  
82 hours of the image acquisition. Representation errors arise where observation  
83 spatial scales are different from the model spatial scale (Janjić et al., 2018).  
84 The spatial resolution of SAR imagery suitable for flood detection varies  
85 across satellite constellation both historically and presently and continues  
86 to improve. Very high resolution (less than 3 m) imaging capabilities are  
87 increasingly available including TerraSAR-X, ALOS-2/PALSAR-2, and the  
88 COSMO-SkyMed, RADARSAT-2, and ICEYE constellations (Mason et al.,  
89 2021a). It is common practice to re-scale SAR-derived flood maps to match  
90 the model grid size for validation or assimilation with model data.

91

92 The objective of this paper is to present a scale-selective approach to eval-  
93 uate flood inundation forecast maps and to develop a physically meaningful  
94 measure of flood-edge location accuracy that can be automated and easily  
95 applied in practice. A new approach is described and applied here to evalu-  
96 ate the spatial scale at which the forecast becomes useful/skilful at capturing  
97 the remotely observed flood extent and specifically the flood-edge location.  
98 The spatial skill of a forecast flood map varies with location. We aim to  
99 improve the conventional contingency map by incorporating the skilful scale  
100 to create a new *categorical scale map*. Also, we address how representation  
101 errors arising from observation spatial scale variations and interpolation have  
102 an impact on model evaluation.

103

104 In the rest of this paper we explore the features of a novel scale-selective  
105 evaluation approach illustrated through application to a case study. In Sec-



106 tion [2](#) we describe the case study, a recent flooding event in the UK following  
107 Storm Dennis, February 2020, along with catchment descriptions for three  
108 chosen domains. The flood inundation forecasting system developed by JBA  
109 Consulting, Flood Foresight, ([Revilla-Romero et al., 2017](#)) is used to produce  
110 forecast flood maps for the event and is detailed in Section [3.1](#). Section [3.2](#)  
111 explains two methods that are used to derive remotely observed flood maps  
112 from SAR imagery. Our new approach to the spatial evaluation of flood maps  
113 is detailed in Section [4](#) along with descriptions of other binary performance  
114 measures. The novel categorical scale map is applied to the case studies in  
115 Section [5](#), and the evaluation results are discussed. We conclude in Section  
116 [6](#) and discuss the wider applications of a spatial scale approach to flood map  
117 skill evaluation.

## 118 **2. Flood event**

119 This extreme flooding event is chosen here as a case study to demonstrate  
120 the features of a spatial scale approach to forecast flood map evaluation.  
121 During February 2020, three named extra-tropical cyclones swept across the  
122 UK in quick succession, each bringing damaging winds and record-breaking  
123 amounts of rainfall ([Met Office, 2020](#)). This led to the River Wye reaching its  
124 highest ever recorded water level at the Old Bridge in Hereford ([riverlevels.uk,](#)  
125 [2020](#)).

### 126 *2.1. Storm Dennis February 2020*

127 Three named storms, Ciara, Dennis and Jorge, arrived in quick succession  
128 during February 2020 delivered by a powerful and ideally positioned jet-  
129 stream that enabled rapid cyclogenesis ([Davies et al., 2020](#)). Each storm

130 rapidly intensified and deepened bringing damaging winds and exceptionally  
131 heavy rainfall across the UK. This month was the UK’s wettest February on  
132 record and the fifth wettest month ever recorded. The UK average rainfall  
133 total exceeded the 1981 – 2010 average by 237% (Kendon, 2020). Locally,  
134 in northwest England and north Wales the rainfall exceedance was three to  
135 four times the typical monthly average rainfall. During this period around  
136 4000 to 5000 properties were flooded in the UK, with significant river water  
137 levels recorded in Wales, west and northwest England (Sefton et al., 2020).  
138 With six days between Ciara and Dennis, groundwater and river levels were  
139 high and soils saturated. The Environment Agency issued a record number  
140 of over 600 flood alerts and warnings for England (JBA, 2021).

## 141 2.2. Catchment location and description

142 Three domains, each differing in hydrological characteristics, have been  
143 selected for forecast flood map evaluation during the storm Dennis flooding  
144 event. Two domains (A and B) have been chosen from the Wye catchment  
145 (Fig. 1). A 28.4 km length centred upon Ross-on-Wye (A) and the Wye at  
146 Hereford (B), a 5.8 km section. A third domain (C) includes 4 km of the  
147 River Lugg.

### 148 2.2.1. The River Wye (domains A and B)

149 The River Wye flows for approximately 215 km from Plynlimon at 750  
150 meters above ordnance datum (mAOD) in the Cambrian Mountains, mid  
151 Wales. It initially travels southeastwards into England where it meanders  
152 southwards to ultimately join the Severn Estuary. The upper catchment  
153 land cover is predominantly grassland with some forest cover with highly im-

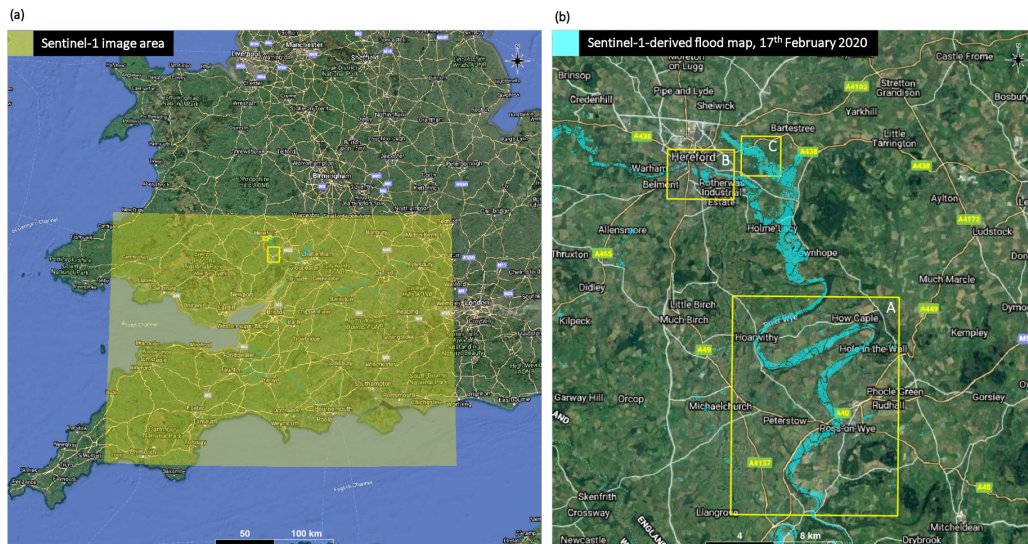


Figure 1: Location of Sentinel-1 image acquisition over southeast UK (a) and flood map evaluation domains (b). Domain A: 28.4 km length of the River Wye centred at Ross-on-Wye, domain size 9.8 x 12.8 km. Domain B: 5.8 km of the River Wye at Hereford, domain size 3.0 x 4.0 km. Domain C: 4 km of the River Lugg at Lugwardine, domain size 2.3 x 2.3 km. Base map from Google Maps.

154 permeable bedrock and superficial deposits of sand and gravel in the Hereford  
 155 area (National River Flow Archive, 2021). The upstream catchment area of  
 156 Hereford is 1896 km<sup>2</sup>. At Hereford, the only city situated on the Wye, the  
 157 river is embanked on the north side by a deep flood wall with further em-  
 158 bankments on the opposite side. Hereford is characterised by the Old Bridge,  
 159 a 15<sup>th</sup> century stone bridge that creates a damming effect during high river  
 160 flows. As the Wye flows south of Hereford, the topography flattens and the  
 161 floodplain widens, with large river meanders and a distinctive U-shaped val-  
 162 ley.

163

164 *2.2.2. River Lugg at Lugwardine (domain C)*

165 The River Lugg has an upstream catchment area of 886 km<sup>2</sup> and a maxi-  
166 mum altitude of 660 mAOD and flows across the grasslands and agricultural  
167 fields of the Herefordshire plain. It has similar bedrock to the Wye catch-  
168 ment and a higher proportion of more permeable superficial fluvial deposits of  
169 sand and gravel. This is particularly evident in the Lugwardine region where  
170 the topography is relatively flat with little to impede the flow of floodwaters  
171 across the plain. The Lugg flows into the River Wye, 2 km south of domain C.  
172

173 *2.2.3. Event hydrology*

174 Daily maximum river levels recorded at Ross-on-Wye, the Old Bridge,  
175 Hereford and Lugwardine for January to March 2020 are plotted in Figure  
176 2 (riverlevels.uk, 2020). The impact of the three storms on the River Wye  
177 is indicated by a very sharp rise in water levels from the 8<sup>th</sup> to the 10<sup>th</sup>  
178 February following storm Ciara. Further heavy showers maintained high wa-  
179 ter levels before storm Dennis brought an exceptional rise in water levels,  
180 peaking on the morning of the 17<sup>th</sup> February with record levels recorded at  
181 Hereford (6.11 m at 9.30 am UCT) and Ross-on-Wye (4.77 m at 5.45 am  
182 UTC). Unfortunately there are two days of missing data at Ross-on-Wye  
183 following the flood event. By analysing the trend between the Hereford and  
184 Ross-on-Wye river levels, the peak level at Ross-on-Wye was likely higher  
185 and later than recorded. The response of the Wye at Hereford is faster than  
186 at Ross-on-Wye, most likely due to the upstream location of Hereford and  
187 a more constrained embankment with the city center located either side of  
188 the river. In comparison to the fast, rapid response of the Wye, the River

189 Lugg displays a distinctively dampened response. Whilst the Lugg initially  
 190 responded quickly to the heavy rainfall, once bankfull was reached and over-  
 191 topping occurred the water levels remained consistently high, with floodwa-  
 192 ters extending across the relatively flat flood plain. The annual exceedance  
 193 probability (AEP) for the recorded peak flow of the Lugg and Wye rivers  
 194 was 0.2 - 0.8 % (return period 120-550 years) and 0.6 - 2.0 % (160-550 years)  
 195 respectively (Sefton et al., 2020).

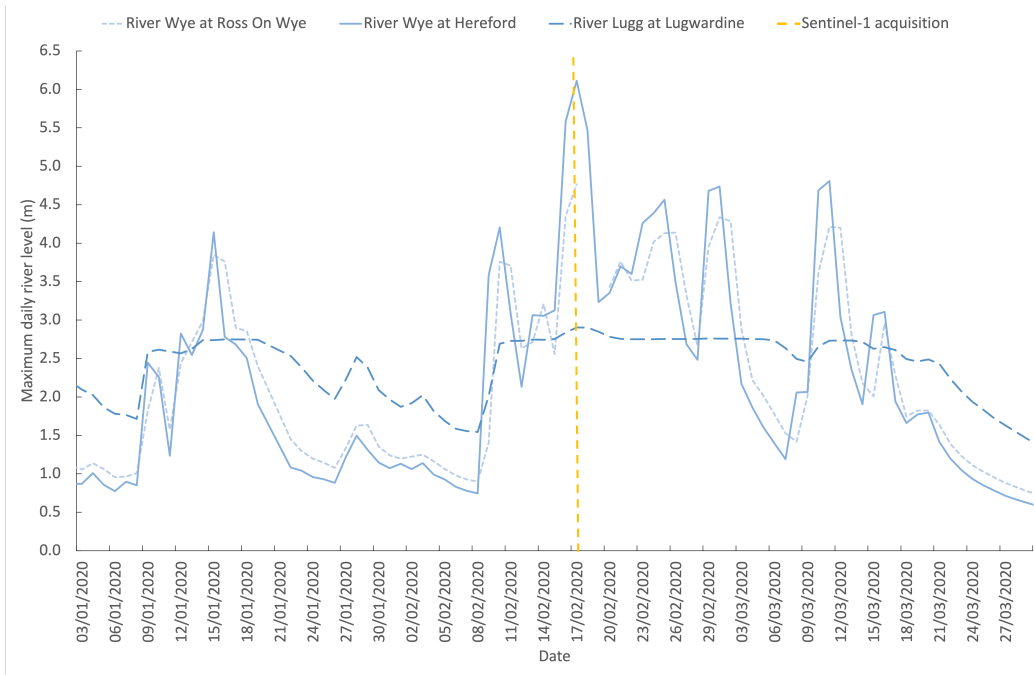


Figure 2: Daily maximum river levels (m) at Ross-on-Wye, Hereford and Lugwardine. The dashed yellow line indicates Sentinel-1 SAR acquisition date.

### 196 **3. Data**

197 In this section we describe the model and observation data that we will  
198 use to illustrate our novel scale selective verification approach.

#### 199 *3.1. Flood Foresight*

200 Flood Foresight (Fig. 3), developed and run routinely by JBA Consulting,  
201 is a fluvial flood inundation mapping system that can be implemented in any  
202 catchment around the globe. Flood Foresight utilises a simulation library  
203 approach to generate maps of real time and forecast flood inundation and  
204 water depth. The simulation library approach saves valuable computing time  
205 and allows the application of Flood Foresight in near continuous real-time at  
206 national and international scales. A library of flood maps is pre-computed  
207 using JFlow<sup>®</sup>, a 2D hydrodynamic model (Bradbrook, 2006). Note that in  
208 this study the flood maps are undefended i.e. temporary flood defences are  
209 not included. JFlow uses a raster-based approach with a detailed underlying  
210 DTM and a simplified form of the full 2D hydrodynamic equations that  
211 capture the main controls of the flood routing for shallow, topographically  
212 driven flow. Five flood maps at 5 m resolution are created for 20, 75, 100, 200  
213 and 1000 year return period flood events (corresponding to annual exceedance  
214 probabilities (AEPs) of 5%, 1.3%, 1%, 0.5% and 0.1% respectively). These  
215 are interpolated to derive five intermediate maps between each adjacent pair  
216 of the JFlow maps, equally spaced in return period creating a total library  
217 of thirty flood maps. Flood Foresight takes inputs of rainfall from numerical  
218 weather prediction (NWP) models, river gauge data (both historical and real-  
219 time) and forecast streamflow and uses these to select the most appropriate

220 flood map for the location and forecast time period. The UK and Ireland  
 221 configurations of the Flood Forecasting Module use deterministic streamflow  
 222 forecast data from the Swedish Meteorological and Hydrological Institute  
 223 (SMHI) European Hydrological Predictions for the Environment (E-HYPE).  
 224 The meteorological input data for the E-HYPE model is the European Centre  
 225 for Medium-range Weather Forecasts (ECMWF) Atmospheric Model high  
 226 resolution (HRES) numerical weather prediction (NWP) model on a 0.1° x  
 227 0.1° grid with forecasts issued daily out to 10 days lead time. Forecast flood  
 228 maps for the UK are produced on a 25 m grid length out to 10 days ahead  
 229 (see [Mason et al. \(2021b\)](#) Section 2.1 for additional details).

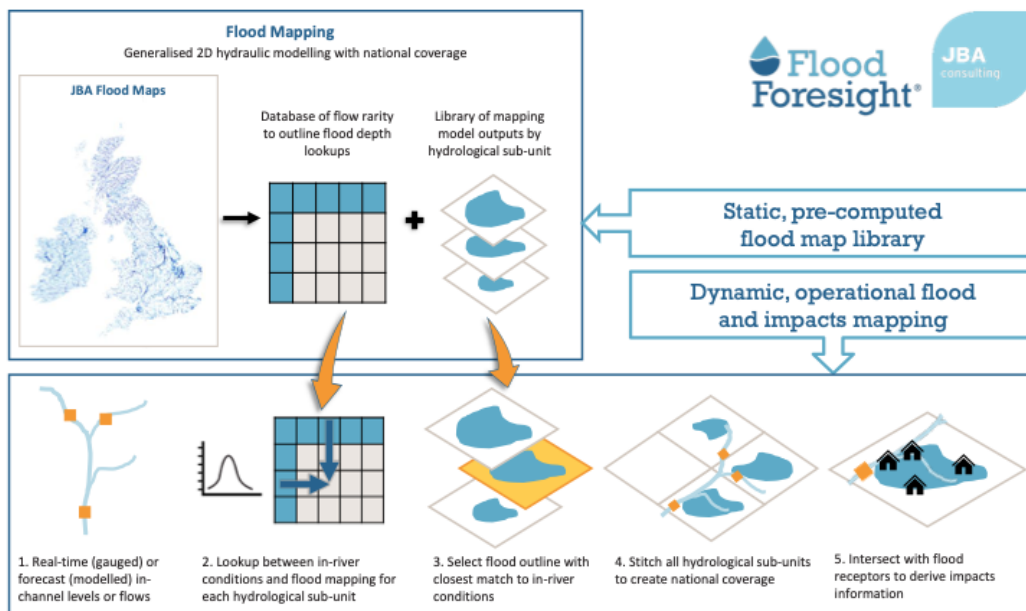


Figure 3: Flood Foresight flood map simulation library selection process. Source JBA Consulting.

230 *3.2. SAR-derived flood maps*

231 Two methods are applied to derive a flood map from SAR backscatter  
232 values captured close to the flood peak. The second method was included  
233 as it provides derivation of flood maps at different spatial resolutions. A  
234 Sentinel-1 (S1B) image was acquired in interferometric wide swath mode  
235 (swath width 250 km) just prior to the flood peak at 0622 on the 17<sup>th</sup> Febru-  
236 ary. A pre-flood image (September 2019) from the same satellite sensor and  
237 track was used to derive the flood map in both methods.

238

239 In the first method, the ESA Grid Processing on Demand (GPOD) HASARD  
240 service (<http://gpod.eo.esa.int/>) has been utilised. The automated flood  
241 mapping algorithm (Chini et al., 2017) uses a statistical, hierarchical split-  
242 based approach to distinguish the two classes (flood and background) using  
243 a pre-flood and flood image. Raw SAR images (VV) are preprocessed, which  
244 involves; precise orbit correction, radiometric calibration, thermal noise re-  
245 moval, speckle reduction, terrain correction, and reprojection to the WGS84  
246 coordinate system. The HASARD mapping algorithm removes permanent  
247 water bodies, including the river water. Flooded areas beneath vegetation,  
248 bridges and near to buildings will not be detected using this method. The  
249 HASARD flood map at 20 m spatial scale is used to evaluate the performance  
250 of Flood Foresight for each of the three domains out to 10 days lead time.

251

252 In the second method, the same Sentinel-1 SAR image (in this case using  
253 both VV and VH) was processed using Google Earth Engine (GEE) to derive  
254 flood maps at a range of spatial resolutions (5 m to 100 m). GEE holds a



255 catalogue of level-1 preprocessed Sentinel-1 SAR images (Google Earth En-  
256 gine Catalog, 2021). A smoothing filter is applied to reduce speckle and a pre  
257 and post flood image are used to train a Classification And Regression Tree  
258 (CART) classifier (Leo Breiman, 1984; Google Earth Engine CART, 2021).  
259 The classifier is applied to the whole image to produce a flood map at a speci-  
260 fied scale. GEE uses an image pyramid approach to scale, or pixel resolution,  
261 analysis. This means variations in the scale selected are determined from the  
262 scale of the input image (Google Earth Engine Scale, 2021). The variation of  
263 the flood extent detected at a range of spatial resolutions and the impact of  
264 re-scaling and interpolation errors on performance measures are investigated.

265

266 Flood Foresight forecast flood maps include the river channel and exclude  
267 surface features such as vegetation and buildings. To smooth the HASARD  
268 and GEE flood maps and allow a fairer comparison we apply a morphological  
269 closing operation (without impacting the location of the flood extent) to flood  
270 fill vegetation and buildings.

#### 271 4. Flood map evaluation methods

272 The following subsections detail a new spatial scale-selective approach to  
273 forecast flood map evaluation. The Fraction Skill Score (FSS) developed by  
274 Roberts and Lean (2008) for validation of convective precipitation forecasts  
275 in atmospheric science uses a neighbourhood approach to determine the scale  
276 at which the forecast becomes skilful. Dey et al. (2016) developed this ap-  
277 proach to determine an agreement scale between an ensemble forecast and  
278 observations at each grid cell to add location specific information. Here we

279 extend the technique to apply it to the new application of flood inundation  
 280 mapping, and further develop a novel categorical scale map that combines  
 281 an agreement scale map with a conventional contingency map.

#### 282 4.1. Spatial scale-selective approach

283 Initially, the observed flood extent derived from SAR data is re-scaled to  
 284 match the forecast flood map grid size using spline interpolation and both  
 285 are converted into binary fields. A threshold approach is determined for the  
 286 situation. For a flood map verification of spatial skill, the simplest example  
 287 applied here is to assign each grid cell as flooded (1) or unflooded (0) for  
 288 the whole domain. Alternative future threshold approaches for flood inun-  
 289 dation maps could include applying thresholds to water depth percentiles.  
 290 The location of the flood-edge cells can be extracted from the observed and  
 291 modelled binary flood maps.

292

293 Given a domain of interest, we number all of the grid cells according to  
 294 their spatial coordinates  $(i, j)$ ,  $i = 1 \dots N_x$  and  $j = 1 \dots N_y$  where  $N_x$  is the  
 295 number of columns in the domain and  $N_y$  is the number of rows. For each grid  
 296 cell a square of length  $n$  forms an  $n \times n$  neighbourhood surrounding the grid  
 297 cell. The fraction of 1s in the square neighbourhood is calculated for each grid  
 298 cell. This creates two fields of fractions over the domain for both the forecast  
 299  $M_{nij}$  and observed  $O_{nij}$  data. The fraction fields are compared against one  
 300 another to calculate the mean squared error (MSE) for the neighbourhood

$$MSE_n = \frac{1}{N_x N_y} \sum_{i=1}^{N_x} \sum_{j=1}^{N_y} [O_{nij} - M_{nij}]^2. \quad (1)$$

301 Based on the fractions calculated for the model and observed fields a worst  
 302 possible MSE is calculated

$$MSE_{n(ref)} = \frac{1}{N_x N_y} \sum_{i=1}^{N_x} \sum_{j=1}^{N_y} [O_{nij}^2 + M_{nij}^2]. \quad (2)$$

303 The FSS is given by

$$FSS_n = 1 - \frac{MSE_n}{MSE_{n(ref)}}. \quad (3)$$

304 Figure 4 illustrates an example of the FSS application at grid level ( $n = 1$ )  
 305 and at the next neighbourhood size  $n = 3$ . In this simple example, there is  
 306 no agreement between the model and observation at grid level but at  $n = 3$ ,  
 307 the skill score improves to 0.92.

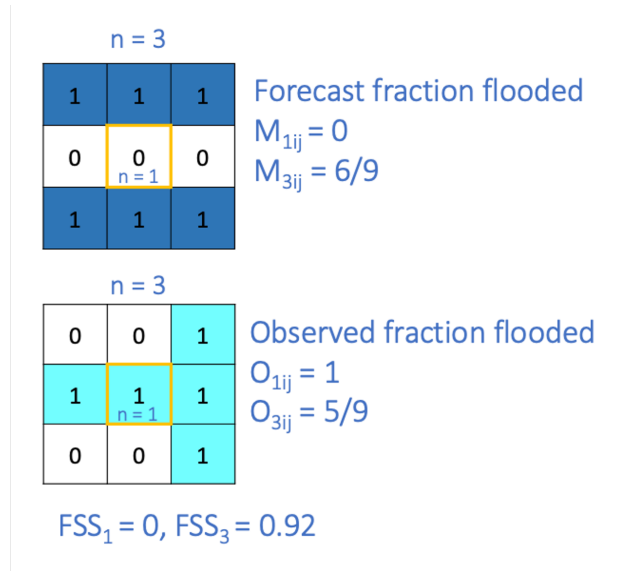


Figure 4: FSS (see subsection 4.1 for calculation details) example applied to a binary flooded (1) / unflooded (0) field at grid scale (yellow box,  $n = 1$ ) and a 3 x 3 neighbourhood (black box,  $n = 3$ ). The observed SAR-derived forecast is in turquoise and the forecast is shown in blue.

308 In general, the FSS is calculated for each length of neighbourhood  $n$ . For  
 309 a given neighbourhood size an FSS of 1 is said to have perfect skill and 0  
 310 means no skill. The FSS will increase as  $n$  increases up to an asymptote  
 311 (see Fig. 3 from [Roberts and Lean \(2008\)](#)). If there is no model bias across  
 312 the whole domain of interest (observed and forecast flooded areas are the  
 313 same) then the asymptotic fraction skill score (AFSS) at  $n = 2N - 1$ , where  
 314  $N$  is the number of points along the longest side of the domain, will equal  
 315 1. Plotting FSS against spatial scale can indicate a range of scales where  
 316 the model is deemed to be the most useful. This usefulness is a trade-off  
 317 between being too smooth (larger  $n$ ) or too fine, where the forecast skill  
 318 is lost and the computation time lengthy. The gradient of the FSS curve  
 319 versus neighbourhood size is another indicator of forecast skill with respect  
 320 to spatial scale. A steeper gradient indicates more rapidly improving skill  
 321 over smaller grid sizes compared with a flatter curve, indicating a much wider  
 322 neighbourhood is required to reach the same skill score. A target FSS score  
 323 ( $FSS_T$ ) is defined as

$$FSS_T \geq 0.5 + \frac{f_o}{2}, \quad (4)$$

324 where  $f_o$  is the fraction of flood observed across the whole domain of interest  
 325 and can be thought of as being equidistant between the skill of a random  
 326 forecast and perfect skill.  $FSS_T$  will vary depending on the magnitude of  
 327 the observed flood, relative to the domain area. This allows the comparison  
 328 of the  $FSS_T$  scale across different domain sizes and floods of different mag-  
 329 nitudes.

330

331 The scale reached at  $FSS_T$  can tell us the displacement distance ( $D_T$ )

332 between the observed and forecast flood, or more meaningfully the flood-edge  
333 locations. As the flood-edge represents a very small fraction of the domain,  
334 the scale at  $FSS_T$  will tend to  $2D_T$ , meaning the displacement distance is  
335 half of this scale (see Figure 4 in [Roberts and Lean \(2008\)](#)).

336

337 It has been shown by [Skok and Roberts \(2016\)](#) that care must be taken  
338 when calculating the FSS near to the domain boundary. After considering  
339 three different ways of treating the boundary, the authors concluded that  
340 as long as the domain was sufficiently large, relative to the spatial errors,  
341 then the boundary effect could be considered to be insignificant. For flood  
342 mapping verification purposes the domain area should be selected to include  
343 the area of interest (e.g. the floodplain) with the neighbourhoods considered  
344 extending beyond the domain at the boundary. This assumes that the obser-  
345 vations available allow this. If this is not that case then another boundary  
346 methods could be applied, such as cropping at the domain edge.

#### 347 *4.2. Location dependent agreement scales*

348 The FSS gives an overall domain averaged measure of forecast perfor-  
349 mance and an average minimum scale at which the forecast is deemed skil-  
350 ful. [Dey et al. \(2016\)](#) describe a method for calculating an agreement scale  
351 at each grid cell located at coordinate position  $(i, j)$ . A brief summary of  
352 the method is presented here. Two fields are considered  $f_{1ij}$  and  $f_{2ij}$ . In this  
353 application these are the forecast and observed fields. In alternative applica-  
354 tions the method could be applied to measure similarity between members  
355 of an ensemble. The fields in this instance are not required to be thresholded  
356 and can be applied to flood depths. The aim is to find a minimum neigh-

357 neighbourhood size (or scale) for every grid point such that there is an agreement  
 358 between  $f_{1ij}$  and  $f_{2ij}$ . This is known as the agreement scale  $S_{ij}$ . The rela-  
 359 tionship between the agreement scale and the neighbourhood size described  
 360 in Section 4.1 is given by  $S_{ij} = (n - 1)/2$ .

361 Firstly, all grid points are compared by calculating the relative MSE  $D_{ij}^S$   
 362 at the grid scale,  $S = 0$  ( $n = 1$ ),

$$D_{ij}^S = \frac{(f_{1ij}^S - f_{2ij}^S)^2}{(f_{1ij}^S)^2 + (f_{2ij}^S)^2}. \quad (5)$$

363 If  $f_{1ij} = 0$  and  $f_{2ij} = 0$  (both dry) then  $D_{ij}^S = 0$  (correct at grid level). Note  
 364 that  $D_{ij}^S$  varies from zero to 1. The fields are considered to be in agreement  
 365 at the scale being tested if:

$$D_{ij}^S \leq D_{crit,ij}^{S_{ij}} \quad \text{where} \quad D_{crit,ij}^S = \alpha + (1 - \alpha) \frac{S}{S_{lim}} \quad (6)$$

366 and  $S_{lim}$  is a predetermined, fixed maximum scale. The parameter value  $\alpha$   
 367 is chosen to indicate the acceptable bias at grid level such that  $0 \leq \alpha \leq 1$ .  
 368 Here we set  $\alpha = 0$  (no background bias). If  $D_{ij}^S \geq D_{crit,ij}^S$  then the next  
 369 neighbourhood size up is considered ( $S = 1$ , a 3 by 3 square). The process  
 370 continues with increasingly larger neighbourhoods until the agreement scale,  
 371 or  $S_{lim}$  is reached for every cell in the domain of interest. The agreement  
 372 scale at each grid cell is then mapped onto the domain of interest.

### 373 4.3. Categorical scale map

374 Currently, the agreement scale map proposed by Dey et al. (2016) pro-  
 375 vides a location-specific scale of agreement between the forecast and observed  
 376 flood map. However, it does not show whether the model is over- or under-  
 377 predicting the flood extent. In our work, we develop the agreement scale

378 map further by combining with a contingency map for the forecast to create  
 379 a new *categorical scale map*. This highlights the agreement scale for areas  
 380 of over- or under-prediction. In a contingency map, each cell in the forecast  
 381 and observed flood map are compared and classified using a contingency ta-  
 382 ble (Table 1). The categories are re-classified numerically in the array for  
 383 automated updating of the agreement scale map. Over-predicted cells (B)  
 384 are set to -1, under-predicted cells (C) are set to +1, correctly predicted  
 385 flooded cells (A) are assigned NaN and correctly predicted unflooded cells  
 386 are set to 0. The array element-wise product of the agreement scale map and  
 387 the numerical contingency map produces the new categorical scale map.

Table 1: Contingency table (based on Stephens et al. (2014)).

|                    | Forecast flooded                   | Forecast unflooded        |
|--------------------|------------------------------------|---------------------------|
| Observed flooded   | A (correct wet)                    | C (under-prediction/miss) |
| Observed unflooded | B (over-prediction/false<br>alarm) | D (correct dry)           |

#### 388 4.4. Binary performance measures

389 It has been suggested by Cloke and Pappenberger (2008) that a range of  
 390 performance measures should be applied so that a forecast can be assessed as  
 391 rigorously as possible. A selection of commonly applied binary performance  
 392 measures, each focusing on a different aspect of performance have been in-  
 393 cluded here for comparison with the Fraction Skill Score results. Following  
 394 the application of a contingency table (Table 1) to the forecast flood map, a  
 395 number of binary performance measures can be calculated (Table 2). Table  
 396 2 describes the range of performance value, the ideal score and a description

397 of which aspects of the forecast flood map performance each binary measure  
398 assesses.

## 399 5. Results and discussion

400 We illustrate and discuss our new method applied to the flood event in  
401 subsection 5.1 and 5.2. The scale-selective approach is applied to an extreme  
402 flooding event in the UK to determine a useful/skilful spatial scale for both  
403 the entire flood extent and the flood-edge location for three domains out  
404 to 10-days lead time. An example forecast flood map for 0-day lead time  
405 compared with the SAR-derived flood map is presented as a contingency  
406 map in Figure 5. The zoomed in perspective shows the double penalty impact  
407 described in Section 1. The discrepancy at the flood-edge depends on the  
408 spatial scale of the forecast flood maps along with the model performance.  
409 Next, in subsection 5.3 location specific agreement scales are presented on  
410 categorical scale maps. The final subsection 5.4 addresses the question of  
411 the impact of representation error caused by variations in SAR-derived flood  
412 map spatial resolution on the evaluation results.

### 413 5.1. Spatial scale variability of forecast flood extent and flood-edge location

414 An evaluation of the spatial skill of the Flood Foresight forecast flood  
415 maps against the SAR-derived flood map for the flood peak on the 17<sup>th</sup>  
416 February 2020 has been calculated for each domain (Fig. 1) for both the en-  
417 tire flood extent and the flood-edge location. The Fraction Skill Score (FSS)  
418 is applied to increasing neighbourhood sizes ( $n$ ) to determine the spatial scale  
419 at which the forecast becomes skilful at capturing the observed flood. Fig-  
420 ure 6 shows FSS against  $n$  for one example, the River Lugg (domain C) for



Table 2: Binary performance measures and formula based on contingency Table [1](#).

| Performance measure                                 | Formula               | Description [range min, range max, perfect score]   |
|---|-----------------------|---|
| Bias  | $\frac{A+B}{A+C}$     | [0, $\infty$ , 1] 1 implies forecast and observed flooded areas are equal > 1 indicates over-prediction, < 1 indicates under-prediction |
| Critical Success Index/Threat score $F^{<2>}$ (CSI) | $\frac{A}{A+B+C}$     | [0, 1, 1] Fraction correct of observed and forecast flooded cells   |
| $F^{<1>}$ Proportion correct                        | $\frac{A+D}{A+B+C+D}$ | [0, 1, 1] Proportion correct (wet and dry) of total domain area   |
| $F^{<3>}$   | $\frac{A-C}{A+B+C}$   | [-1, 1, 1] Score reduced by over-prediction   |
| $F^{<4>}$   | $\frac{A-B}{A+B+C}$   | [-1, 1, 1] Score reduced by under-prediction  |
| False Alarm Rate (FAR)                              | $\frac{B}{B+D}$       | [0, 1, 0] Proportion of over-prediction of dry areas  |
| Hit Rate (HR)                                       | $\frac{A}{A+C}$       | [0, 1, 1] Fraction correct of observed flooded area   |
| Pierce Skill Score (PSS)                            | $HR - FAR$            | [-1, 1, 1] Incorporates both under and over-prediction  |

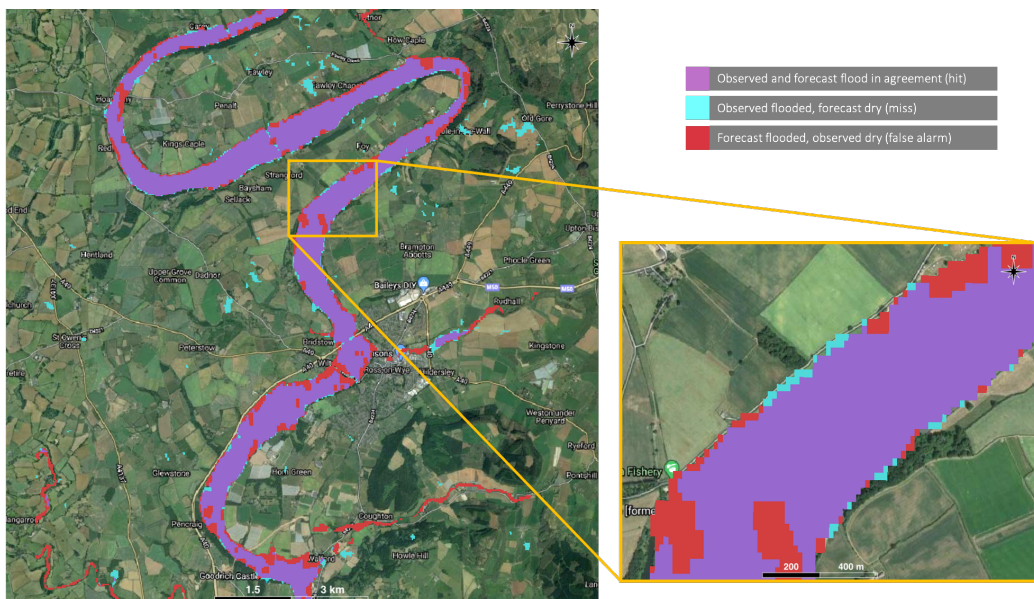


Figure 5: Left panel: contingency map of a 0-day lead time forecast versus the HASARD SAR-derived flood map for the Wye valley indicates the model is predicting the flood extent accurately, including the position of the flood-edge. Right panel: Zoom of yellow box on the left panel. On closer inspection, at grid level, the flood-edge in many places is over- or under-predicted by around one grid length. Base map from Google Maps.

421 the entire flood (a) and the flood-edge (b). Each line represents a different  
 422 model run date from the 10/02/2020 (7-day lead time) to the 17/02/2020  
 423 (0-day lead time). With the exception of the 7-day lead time, all forecasts  
 424 for the whole flood (Fig. 6a) exceed the  $FSS_T$  at grid level ( $n = 1$ ) with  
 425 gradually improving skill as  $n$  increases. In contrast to this, the FSS applied  
 426 to the flood-edge (Fig. 6b) shows all forecasts below  $FSS_T$  at grid level and  
 427  $n = 3$  with the skill increasing more rapidly compared with the whole flood  
 428 to reach  $FSS_T$  at  $n = 5$  for all run dates within a 5-day lead time (except for  
 429 16/02/2020, which is just below  $FSS_T$ ). This indicates that the flood-edge

430 is forecast to be around 62.5 m from the observed flood-edge, on average,  
 431 for a 5-day lead time. The difference between the gradients of the plots in-  
 432 dicate the flood-edge is more sensitive to changes in spatial scale compared  
 433 with evaluation of the whole flooded area. The whole flood verification here  
 434 indicates a strong model performance. However, verifying the whole flood  
 435 alone could mask the flood-edge location performance, which in this case has  
 436 a coarser scale at  $FSS_T$ . Similar trends in FSS with neighbourhood size and  
 437 comparisons between the entire flood and the flood-edge verification scales  
 438 are found for all domains. The rate of FSS increase, or FSS gradient with  
 439  $n$ , tells us how quickly the forecast skill improves with increasing scale. A  
 440 more spatially accurate forecast of the flood-edge will demonstrate a steeper  
 441 gradient, reaching  $FSS_T$  at a smaller neighbourhood size.

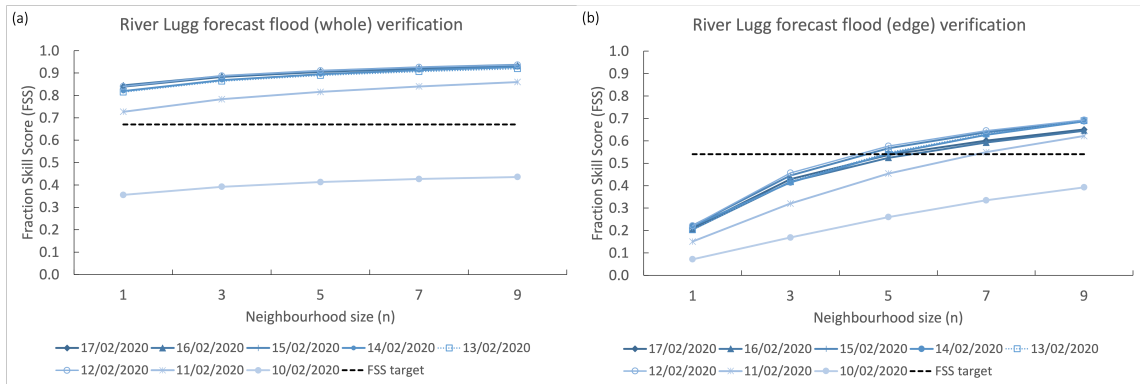


Figure 6: FSS calculated for the River Lugg at Lugwardine for (a) entire flood extent and (b) the flood-edge for increasing neighbourhood sizes for daily forecast lead times up to 7 days.

442 5.2. Comparison of spatial scales at differing lead times and domain location

443 The performance measures for each domain for daily lead times out to 10  
444 days are presented in Figure 7. The FSS at  $n = 1, 3,$  and 5 are shown along  
445 with Critical Success Index (CSI), Hit Rate (HR), Pierce Skill Score (PSS)  
446 and the Bias (see Table 2 for definitions). The Bias score is an indicator  
447 of over- or under-prediction of the flood extent and is plotted on a separate  
448 axis to account for the larger range. For lead times within 5-days of the  
449 flood peak,  $FSS > 0.8$  for the entire flooded area at grid level for the River  
450 Wye (domain A) indicates a strong model performance (Fig. 7a). There is a  
451 dip in the FSS on the 16/02/2020 where the forecast over-predicts the flood  
452 extent. This is also reflected in the CSI score. In contrast to this the HR and  
453 PSS increase, despite the over-prediction, as more observed flood cells are  
454 correctly predicted wet. We note that the PSS (HR - FAR) does account for  
455 over-prediction, however the FAR is the fraction of the dry area incorrectly  
456 predicted wet, which is very small relative to the HR (0.03 versus 0.90). Val-  
457 idation of the River Wye flood-edge (Fig. 7b) is more sensitive to changes  
458 in neighbourhood size compared with the whole flood validation. Here the  
459 flood-edge is very well forecast in terms of spatial location and exceeds  $FSS_T$   
460 at  $n = 3$  (on average, 37.5 m displacement) for a 5-day lead time (except for  
461 1-day lead time where  $FSS_T$  is exceeded at  $n = 5$ ). As shown previously in  
462 Subsection 5.1, the forecast of the River Lugg flood-edge is skilful at  $n = 5$   
463 (Fig. 7f) (on average, 62.5 m displacement) for a 5-day lead time. Differences  
464 in the hydrological characteristics might explain differences in model perfor-  
465 mance. The Wye valley flood plain is well defined with distinctive valley  
466 sides and this event proved to be valley filling in contrast to the Lugg flood

467 plain which is relatively flat and extensive. This could explain the increased  
468 skill shown for the prediction of the Wye flood-edge. The average observed  
469 flood top width for the Lugg (domain C) is 740 m and for the Wye (domain  
470 A) 430 m. This gives a flood-edge displacement as a fraction of the flood top  
471 width of 7.4% for the Lugg and 7.8% for the Wye.

472

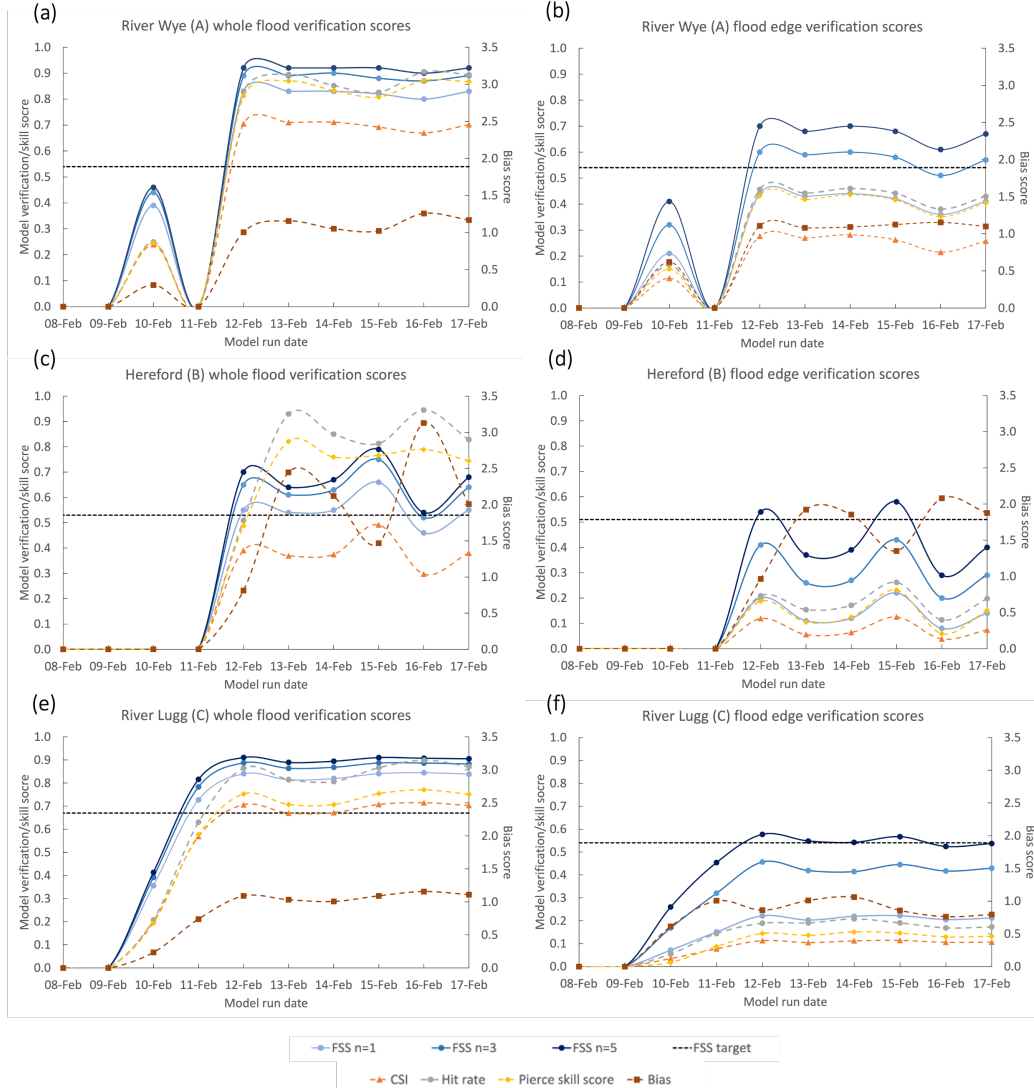


Figure 7: Conventional binary performance measures (dashed lines) and FSS (solid lines) at  $n = 1, 3,$  and  $5$  for each domain for both the whole flooded area and the flood-edge for daily lead times out to 10 days for the River Wye (domain A, (a) and (b)), Hereford (domain B, (c) and (d)) and the River Lugg (domain C, (e) and (f)). Plots on the left show the verification scores applied to the entire flood extent and plots on the right show the flood-edge scores.

473 There is more variation in skilful scale with lead time evident for the Wye  
474 at Hereford (domain B) in Figure 7c and d compared with domain A and  
475 C. To achieve the same FSS for the whole flood as domain A and C up to a  
476 5-day lead time, the neighbourhood size would need to exceed  $n = 5$ . The  
477 model is over-predicting the flood extent, in particular on the 16/02/2020  
478 (1-day) lead time. This overprediction at 1-day lead time is evident for all  
479 domains as can be seen in the Bias scores but the impact of this is most  
480 noticeable at Hereford. Hereford has more complex topography compared to  
481 the other domains, particularly along the river bank with bridges, buildings,  
482 permanent and temporary flood defences deployed during the event affecting  
483 the flow of the flood wave through the city. The maps used in the simulation  
484 library of Flood Foresight are produced using a bare-earth DTM. Despite  
485 this, the model performs well, exceeding  $FSS_T$  at  $n = 5$  at the 5-day and  
486 2-day lead times for the flood-edge forecast.

487

488 Overall, the FSS indicates a similar trend in performance across all results  
489 as the commonly applied CSI. The value of  $FSS_T$  is determined by the  
490 magnitude of the observed flood, which means the skilful scale determined  
491 at  $FSS_T$  can be meaningfully compared across the domains. The skilful scale  
492 of the forecast flood-edge location gives an average discrepancy distance. A  
493 physically meaningful evaluation measure provides additional information  
494 compared to a conventional verification score.

### 495 5.3. Categorical scale maps

496 Location dependent categorical scale maps (Subsection 4.3) have been  
497 calculated for all run dates for both the entire flooded area and the flood-

498 edge. Figure 8 shows categorical scale maps for the whole flood for three  
499 different lead times for each domain, longer lead times are on the left. The  
500 run dates vary with domain to present the most informative maps such  
501 that variation in forecast skill can be seen across the different lead times.  
502 The colours on the map indicate grid cell specific agreement scales (Subsec-  
503 tion 4.2) between the forecast flood map and the SAR-derived flood map.  
504 Grey/white regions indicate correctly predicted flooded/unflooded cells, red  
505 shows the forecast flood extent is under-predicted (miss) and blue indicates  
506 over-prediction (false alarm). Increasingly darker shades of red/blue show  
507 that larger scales were needed for the agreement criteria to be met. The dark-  
508 est blue at  $S = 10$  indicates a total mismatch between forecast and observed  
509 flooding. The addition of the agreement scale information in comparison to a  
510 conventional contingency map (for an example, see Fig. 5) quickly highlights  
511 regions of total mismatch through the darkest shading, with areas that are  
512 slightly misaligned in lighter shades. The agreement scale indicated gives a  
513 physical measure of distance at specific locations between the forecast and  
514 the observed flood map (where  $S < S_{lim}$ ).

515

516 The location specific skilful scale varies with location and lead time as  
517 indicated on the categorical scale maps. For a 7-day lead time forecast for  
518 the River Wye (Fig. 8a), the model is indicating some flooding could occur,  
519 although under-estimating the total extent as show by the darkest red areas,  
520 which show the limits of the agreement scale have been reached. By 5-days  
521 lead time the forecast is in very close agreement with the observed flood at  
522 grid level (in grey) with larger agreement scales indicated by red/blue shad-



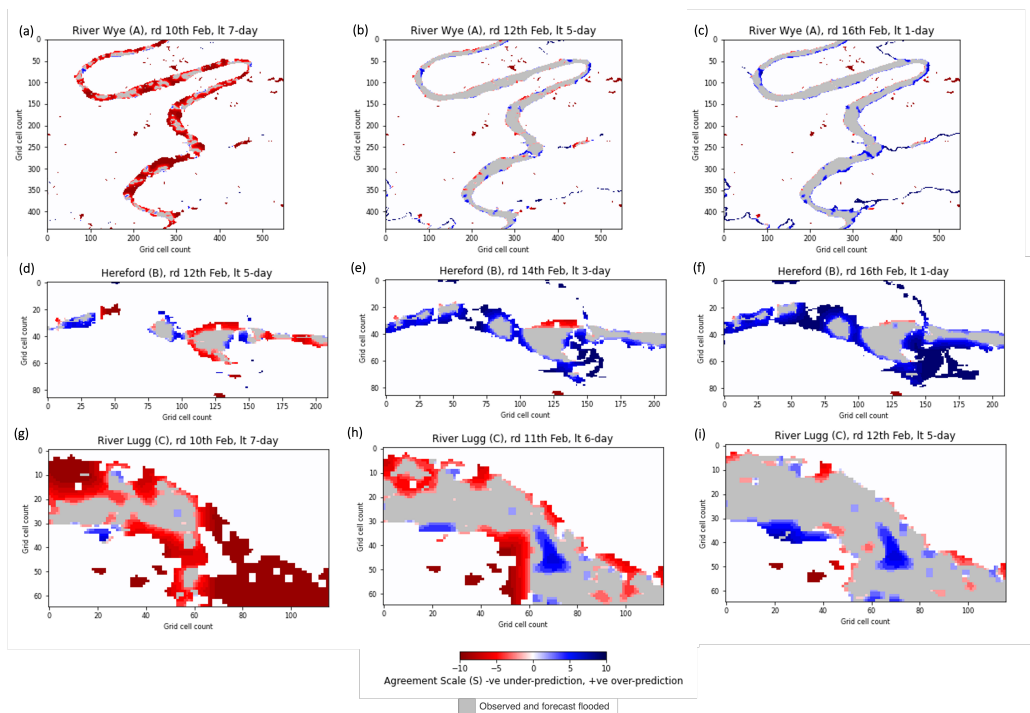


Figure 8: Categorical scale maps for each domain at various lead times (lt). Red indicates where the forecast flood extent is under-predicted, blue indicates over-prediction. The shading indicates the agreement scale, a measure of distance between the forecast and observed flood maps. Grey areas are correctly predicted flooded, white areas are correctly predicted unflooded. Each grid cell represents 25 m x 25 m for all domains. (Note: rd (forecast run date) varies between location, all dates have been evaluated and the most illustrative maps selected.)

523 ing along some of the flood-edge locations (Fig. 8b) and a balance between  
 524 under- and over-prediction. Over-prediction is more evident by 1-day lead  
 525 time for the River Wye (Fig. 8c). The Hereford forecast is most skilful on  
 526 the 12<sup>th</sup> February (Fig. 8d) with over-prediction, particularly towards the  
 527 southwest at 3-day and 1-day lead times (Fig. 8e and f). A small stream  
 528 running southwards to the Wye, the Eign Brook, could be contributing to the

529 over-prediction seen here. It is also worth mentioning that SAR will struggle  
530 to detect flood waters where buildings are closer together when the distance  
531 between them is less than the ground resolution of the SAR. Shadow and  
532 layover effects due to the side-looking nature of the SAR also mean flood  
533 detection is more difficult in urban areas (Mason et al., 2021a). This will  
534 likely only impact a small area of the Hereford domain but this observation  
535 uncertainty should be considered when interpreting these results. There is  
536 an area of under-prediction of the flood extent in the centre of the Hereford  
537 domain visible at all lead times. This could be due to surface water flooding,  
538 which most likely occurred due to the very high intensity rainfall observed.  
539 This combined with the urban area and steeply sloping gradient to the north  
540 of this area most likely contributed to rapid surface water runoff towards the  
541 river. Since Flood Foresight is a fluvial flooding forecast system we would  
542 not expect surface water flooding such as this to be predicted.

543

544 Flood Foresight selects multiple flood maps and stitches them together  
545 when the return period threshold is exceeded for a given area. The Hereford  
546 section of the Wye does not trigger a flood map selection until a 5-day lead  
547 time, this area also influences part of the River Lugg flood map and can be  
548 seen as a mismatch on the lower left hand side of Figure 8g and h. Once  
549 this is included the forecast flood map is in very good agreement from a 5-  
550 day lead time. There are areas that could be further improved, indicated by  
551 the lighter shading (Fig. 8i). An acceptable level of agreement scale could  
552 be determined for a given situation, for example  $n < 5$ , and efforts made  
553 to understand/improve larger agreement scales at specific locations. These

554 improvements might include changes to infrastructure included in the DTM  
555 used in the hydraulic modelling, for example.

#### 556 *5.4. SAR-derived flood map scale variation*

557 Here we address the question of how varying spatial resolution of SAR-  
558 derived flood maps affects the scale selective skill scores. SAR-derived flood  
559 maps produced using a CART classifier in GEE at spatial resolutions from  
560 5 m to 100 m are re-scaled by 0-order spline interpolation (`ndimage.zoom`,  
561 `2021`; Briand and Monasse, `2018`) to match the model resolution (25 m) and  
562 compared to the forecast flood map for the River Lugg (5-day lead time). A  
563 comparison of the GEE flood map against the HASARD flood map, both at  
564 20 m spatial scale produce almost identical verification scores for all perfor-  
565 mance measures for the River Lugg ( $\Delta FSS < 0.01$ ).

566  
567 The 25 m GEE flood map is taken to be the reference flood extent. The  
568 impact of higher or lower scale flood observation on over/under-prediction of  
569 the flood extent can be evaluated by comparing the difference between higher  
570 resolution (HR) flood maps (5, 10 and 20 m) with the reference map, and  
571 lower resolution (LR) flood maps (30, 50, 75, and 100 m) with the reference  
572 map. The results presented in Table `3` are calculated by comparing the flood  
573 maps using the contingency table (Table `1`). Overall, the HR maps show a  
574 higher percentage agreement with the reference map relative to the LR maps.  
575 Higher resolution flood maps (5 or 10 m) show speckling or noise away from  
576 the main flood extent, which contributes to their over-estimation (relative  
577 to under-estimation) of the extent. Conversely, a coarser image will lead to  
578 additional under-estimation of the flood extent (relative to over-estimation)

579 and a greater overall proportional error compared to higher resolution maps.

580

Table 3: Comparison of SAR-derived flood map at various spatial resolutions against the SAR-derived 25 m reference flood map. The difference between the SAR-derived flood map and the reference map was calculated to determine the over- and under-estimation.

| Spatial resolution (m) | Agreement (%) | Over-estimation (%) | Under-estimation (%) | Estimation tendency |
|------------------------|---------------|---------------------|----------------------|---------------------|
| 5                      | 94.87         | 2.72                | 2.41                 | over                |
| 10                     | 94.16         | 3.94                | 1.90                 | over                |
| 20                     | 95.02         | 2.65                | 2.33                 | over                |
| 30                     | 94.16         | 2.92                | 2.91                 | balanced            |
| 50                     | 89.65         | 4.45                | 5.90                 | under               |
| 75                     | 90.22         | 3.46                | 6.32                 | under               |
| 100                    | 84.8          | 4.86                | 10.33                | under               |

581 The impact of differing SAR flood map spatial scales along with errors due  
582 to interpolation on model verification can be seen in the agreement scale maps  
583 (Fig. 9). Along the northern flood-edge, the apparent emphasis changes  
584 from model under-prediction (red) in (a) to (e), to over-prediction (blue) in  
585 (f) to (h). The resulting skill scores for the same 5-day forecast flood map  
586 against the initial SAR-derived flood map scale are displayed in Figure 10.  
587 The highest skill scores are achieved for the whole flood verification when  
588 the SAR-derived flood map is produced at the same scale as the model.  
589 This requires no additional interpolation. A slight increase or decrease in  
590 observation scale from this by 5 m reduces the forecast skill score. The

591 apparent model skill drops more significantly beyond an observation scale  
 592 of 50 m and this is more evident in the whole flood compared to the flood-  
 593 edge verification. The skilful scale of the flood-edge (Fig. 10b) remains at  
 594  $n = 5$  until it exceeds this when the SAR-derived flood map resolution is  
 595 greater than 80 m. Observation scale selection and re-scaling along with  
 596 interpolation errors must be considered when evaluating model performance,  
 597 particularly where model or observation scales vary in space and time, or  
 598 where comparisons are made across different models.

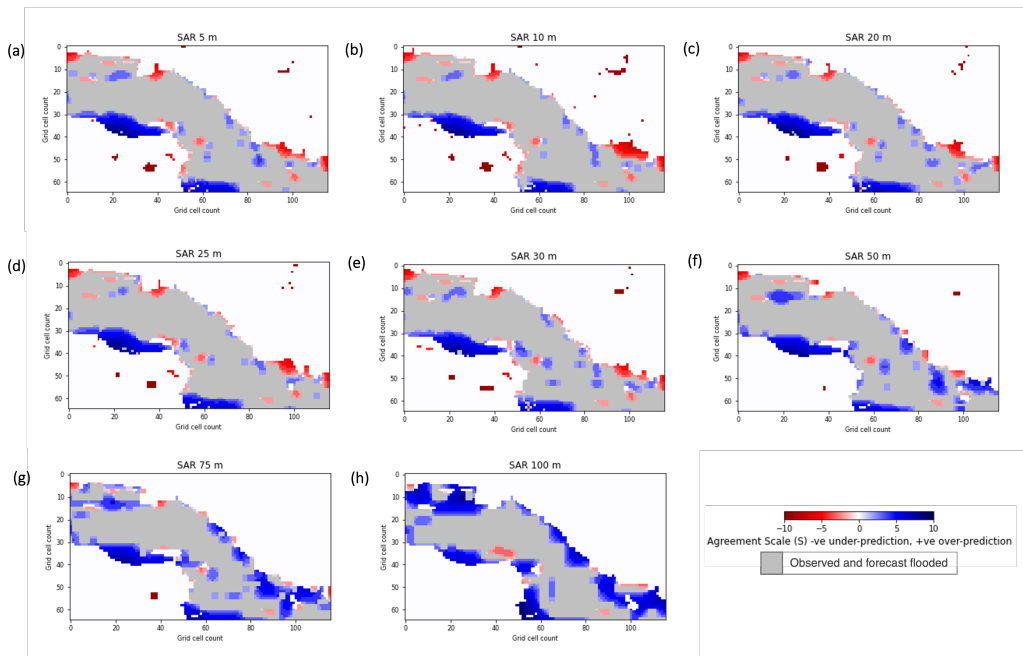


Figure 9: SAR-derived flood maps produced at different spatial resolutions (5 m to 100 m) are re-scaled to the model grid size (25 m) before categorical scale maps are calculated for the River Lugg (C), rd 12th Feb.

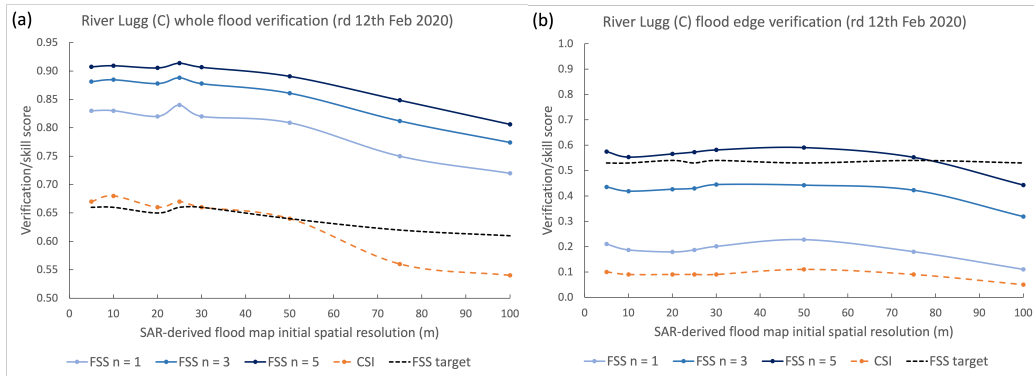


Figure 10: SAR-derived flood maps at different spatial resolutions (5 m to 100 m) are re-scaled to the model grid size (25 m) before verification scores are calculated for the whole flood (a) and the flood-edge (b).

## 599 6. Conclusions

600 Overall, the aim of this paper was to introduce and apply a new scale-  
 601 selective approach to forecast flood map evaluation with an emphasis on pro-  
 602 viding a physically meaningful verification of the flood-edge location. The  
 603 skilful spatial scale for comparison of forecast flood inundation maps against  
 604 SAR-derived observed flood extent has been evaluated by the application of  
 605 the Fraction Skill Score: this provides a domain averaged skilful scale. The  
 606 verification measure has been applied to a forecast of an extreme flood event  
 607 in the UK on the River Wye and the River Lugg following Storm Dennis in  
 608 February 2020. Flood Foresight inundation predictions with lead times out  
 609 to 10 days are evaluated against a Sentinel-1 SAR-derived flood map cap-  
 610 tured close to the flood peak for three domains, each differing in hydrological  
 611 characteristics. Conventional binary performance measures were calculated  
 612 alongside the FSS for comparison. Flood-edge verification shows greater sen-

613 sitivity to changes in forecast skill and spatial scale, relative to verification of  
614 the entire flood extent. The skilful scale determined is physically meaningful  
615 and can be used to estimate the average flood-edge discrepancy from the ob-  
616 served flood-edge. The observed flood map spatial resolution relative to the  
617 model scale is important and re-scaling and interpolation errors will impact  
618 the model verification scores. Ideally, the observed flood map should be de-  
619 rived at the same spatial scale as the forecast model to minimise these errors.

620

621 In operational practice the scale at which the forecast flood maps are  
622 presented to forecasters and decision makers should reflect the uncertainty  
623 within the forecast. Very high resolution flood maps can be presented where  
624 a detailed DTM is available. If this is presented as a deterministic forecast  
625 to flood risk management teams, it could lead to an over confidence in the  
626 forecast, or where the actual observed flood magnitude is different, the fore-  
627 cast may be devalued in the future (Speight et al., 2021). Application of a  
628 spatial-scale approach to forecast evaluation can determine the scale at which  
629 it is best to present the forecast flood map. Conversely, if the model is found  
630 to be skilful at grid level, there is scope to increase the flood map resolu-  
631 tion adding more detail to the flood-edge location. Improvements made to  
632 hydrodynamic models, such as through data assimilation to improve inputs,  
633 initial conditions or model parameters may not improve the forecast flood-  
634 edge location at grid level. However, improvements may be evident through  
635 evaluation using FSS across a range of scales. Categorical scale maps are a  
636 useful evaluation and forecasting tool, adding location specific detail. Model  
637 improvements can be spatially targeted and as improvements are made, the

638 categorical scale map will highlight location specific changes. For example,  
639 the categorical scale maps for Hereford indicate the local infrastructure (in  
640 particular bridges) impact the movement of the flood wave, which suggests  
641 a digital surface model (DSM) would be beneficial in urban areas.

642

643 The spatial-scale approach will also prove a useful tool in multi-model  
644 performance comparisons where forecast flood maps are presented at differ-  
645 ent spatial resolutions or to evaluate the performance of an increase in model  
646 resolution. Evaluating a skilful scale for each model can be compared di-  
647 rectly whereas the skill score values should not be compared across models  
648 with different spatial scales (Emerton et al., 2016). These methods will also  
649 benefit surface water flooding verification where the flood map is likely to  
650 be localised and discrete and accounting for variations in spatial skill more  
651 critical. An improved approach to evaluating forecast flood maps will result  
652 in improved accuracy in the predictions of flooding. Ultimately, this will  
653 benefit disaster management teams and those living in flood prone areas to  
654 enable future mitigation of flooding impacts.

655

656 Acknowledgements

657 Funding: This work was supported in part by the Natural Environment Re-  
658 search Council as part of a SCENARIO funded PhD project with a CASE  
659 award from the JBA Trust (NE/S007261/1). Sarah L Dance and David C  
660 Mason were funded in part by the UK EPSRC DARE project (EP/P002331/1).  
661 Sarah L Dance also received funding from NERC National Centre for Earth  
662 Observation.



663

664 Code and data availability: The functions used to evaluate the forecast  
665 flood maps using a scale-selective approach along with the SAR-derived and  
666 forecast flood maps are available on the following Zenodo page: [https:](https://doi.org/10.5281/zenodo.6011882)  
667 [//doi.org/10.5281/zenodo.6011882](https://doi.org/10.5281/zenodo.6011882) (Hooker, H., 2022).

668

669 **References**

- 670 Bradbrook, K., 2006. JFLOW: A multiscale two-dimensional dynamic flood  
671 model. *Water and Environment Journal* doi:[10.1111/j.1747-6593.2005.](https://doi.org/10.1111/j.1747-6593.2005.00011.x)  
672 [00011.x](https://doi.org/10.1111/j.1747-6593.2005.00011.x).
- 673 Briand, T., Monasse, P., 2018. Theory and practice of image B-spline interpo-  
674 lation. *Image Processing On Line* 8, 99–141. doi:[10.5201/ipol.2018.221](https://doi.org/10.5201/ipol.2018.221).
- 675 Briggs, W.M., Levine, R.A., 1997. Wavelets and field forecast verification.  
676 *Monthly Weather Review* 125, 1329–1373. doi:[10.1175/1520-0493\(1997\)](https://doi.org/10.1175/1520-0493(1997)125<1329:waffv>2.0.co;2)  
677 [125<1329:waffv>2.0.co;2](https://doi.org/10.1175/1520-0493(1997)125<1329:waffv>2.0.co;2).
- 678 Casati, B., Wilson, L.J., 2007. A new spatial-scale decomposition of the brier  
679 score: Application to the verification of lightning probability forecasts.  
680 *Monthly Weather Review* 135, 3052–3069. doi:[10.1175/MWR3442.1](https://doi.org/10.1175/MWR3442.1).
- 681 Chini, M., Hostache, R., Giustarini, L., Matgen, P., 2017. A hierarchical  
682 split-based approach for parametric thresholding of SAR images: Flood  
683 inundation as a test case. *IEEE Transactions on Geoscience and Remote*  
684 *Sensing* 55, 6975–6988. doi:[10.1109/TGRS.2017.2737664](https://doi.org/10.1109/TGRS.2017.2737664).
- 685 Cloke, H.L., Pappenberger, F., 2008. Evaluating forecasts of extreme events  
686 for hydrological applications: An approach for screening unfamiliar perfor-  
687 mance measures, in: *Meteorological Applications*. doi:[10.1002/met.58](https://doi.org/10.1002/met.58).
- 688 Cooper, E.S., Dance, S.L., García-Pintado, J., Nichols, N.K., Smith, P.J.,  
689 2019. Observation operators for assimilation of satellite observations in  
690 fluvial inundation forecasting. *Hydrology and Earth System Sciences* 23,  
691 2541–2559. doi:[10.5194/hess-23-2541-2019](https://doi.org/10.5194/hess-23-2541-2019).

692 Copernicus Programme, 2021. Copernicus Emergency Management Service.  
693 <https://emergency.copernicus.eu/>, last access 14th September 2021.

694 Dasgupta, A., Grimaldi, S., Ramsankaran, R.A., Pauwels, V.R., Walker, J.P.,  
695 2018. Towards operational SAR-based flood mapping using neuro-fuzzy  
696 texture-based approaches. *Remote Sensing of Environment* 215, 313–329.  
697 doi:[10.1016/j.rse.2018.06.019](https://doi.org/10.1016/j.rse.2018.06.019).

698 Dasgupta, A., Hostache, R., Ramsankaran, R., Schumann, G.J., Grimaldi,  
699 S., Pauwels, V.R.N., Walker, J.P., 2021a. On the impacts of observation  
700 location, timing and frequency on flood extent assimilation performance.  
701 *Water Resources Research* doi:[10.1029/2020wr028238](https://doi.org/10.1029/2020wr028238).

702 Dasgupta, A., Hostache, R., Ramsankaran, R.A., Schumann, G.J., Grimaldi,  
703 S., Pauwels, V.R., Walker, J.P., 2021b. A Mutual Information-Based Like-  
704 lihood Function for Particle Filter Flood Extent Assimilation. *Water Re-  
705 sources Research* 57, 1–28. doi:[10.1029/2020WR027859](https://doi.org/10.1029/2020WR027859).

706 Davies, P.A., Mccarthy, M., Christidis, N., Dunstone, N., Knight, J.R.,  
707 Adam, A., 2020. The wet and stormy UK winter of 2019 / 2020 , 1–  
708 7doi:[10.1002/wea.3955](https://doi.org/10.1002/wea.3955).

709 Dey, S.R., Leoncini, G., Roberts, N.M., Plant, R.S., Migliorini, S., 2014.  
710 A spatial view of ensemble spread in convection permitting ensembles.  
711 *Monthly Weather Review* doi:[10.1175/MWR-D-14-00172.1](https://doi.org/10.1175/MWR-D-14-00172.1).

712 Dey, S.R., Roberts, N.M., Plant, R.S., Migliorini, S., 2016. A new method  
713 for the characterization and verification of local spatial predictability for

714 convective-scale ensembles. Quarterly Journal of the Royal Meteorological  
715 Society doi:[10.1002/qj.2792](https://doi.org/10.1002/qj.2792).

716 Di Mauro, C., Hostache, R., Matgen, P., Pelich, R., Chini, M., van Leeuwen,  
717 P.J., Nichols, N., Blöschl, G., 2020. Assimilation of probabilistic flood  
718 maps from SAR data into a hydrologic-hydraulic forecasting model: a  
719 proof of concept. Hydrology and Earth System Sciences Discussions , 1–  
720 24doi:[10.5194/hess-2020-403](https://doi.org/10.5194/hess-2020-403).

721 Emerton, R.E., Stephens, E.M., Pappenberger, F., Pagano, T.C., Weerts,  
722 A.H., Wood, A.W., Salamon, P., Brown, J.D., Hjerdt, N., Donnelly,  
723 C., Baugh, C.A., Cloke, H.L., 2016. Continental and global scale flood  
724 forecasting systems. Wiley Interdisciplinary Reviews: Water 3, 391–418.  
725 doi:[10.1002/wat2.1137](https://doi.org/10.1002/wat2.1137).

726 Environment Agency, 2021. National LIDAR Programme. [https://](https://data.gov.uk/dataset/f0db0249-f17b-4036-9e65-309148c97ce4/national-lidar-programme)  
727 [data.gov.uk/dataset/f0db0249-f17b-4036-9e65-309148c97ce4/](https://data.gov.uk/dataset/f0db0249-f17b-4036-9e65-309148c97ce4/national-lidar-programme)  
728 [national-lidar-programme](https://data.gov.uk/dataset/f0db0249-f17b-4036-9e65-309148c97ce4/national-lidar-programme), last access 29<sup>th</sup> April 2021.

729 García-Pintado, J., Mason, D.C., Dance, S.L., Cloke, H.L., Neal, J.C.,  
730 Freer, J., Bates, P.D., 2015. Satellite-supported flood forecasting in  
731 river networks: A real case study. Journal of Hydrology 523, 706–724.  
732 doi:[10.1016/J.JHYDROL.2015.01.084](https://doi.org/10.1016/J.JHYDROL.2015.01.084).

733 GFM, 2021. GloFAS Global Flood Monitoring (GFM). [https://](https://www.globalfloods.eu/technical-information/glofas-gfm/)  
734 [www.globalfloods.eu/technical-information/glofas-gfm/](https://www.globalfloods.eu/technical-information/glofas-gfm/), last ac-  
735 cess 28th October 2021.

736 Google Earth Engine CART, 2021. ee.Classifier.smileCart.  
737 <https://developers.google.com/earth-engine/apidocs/>  
738 [ee-classifier-smilecart](https://developers.google.com/earth-engine/apidocs/ee-classifier-smilecart), last access 29th April 2021.

739 Google Earth Engine Catalog, 2021. Sentinel Collection. [https:](https://developers.google.com/earth-engine/datasets/catalog/)  
740 [//developers.google.com/earth-engine/datasets/catalog/](https://developers.google.com/earth-engine/datasets/catalog/)  
741 [COPERNICUS\\_S1\\_GRD](https://developers.google.com/earth-engine/datasets/catalog/COPERNICUS_S1_GRD), last access 4<sup>th</sup> August 2021.

742 Google Earth Engine Scale, 2021. Image Pyramids. [https://developers.](https://developers.google.com/earth-engine/guides/scale)  
743 [google.com/earth-engine/guides/scale](https://developers.google.com/earth-engine/guides/scale), last access 16<sup>th</sup> September  
744 2021.

745 Grimaldi, S., Li, Y., Pauwels, V.R., Walker, J.P., 2016. Remote Sensing-  
746 Derived Water Extent and Level to Constrain Hydraulic Flood Forecasting  
747 Models: Opportunities and Challenges. *Surveys in Geophysics* 37, 977–  
748 1034. doi:[10.1007/s10712-016-9378-y](https://doi.org/10.1007/s10712-016-9378-y).

749 Hagen, A., 2003. Fuzzy set approach to assessing similarity of categorical  
750 maps. *International Journal of Geographical Information Science* 17, 235–  
751 249. doi:[10.1080/13658810210157822](https://doi.org/10.1080/13658810210157822).

752 Hooker, H., 2022. Spatial scale evaluation of forecast flood inundation maps  
753 (v1.0) [Data set]. zenodo. <https://doi.org/10.5281/zenodo.6011881>,  
754 last access 8th February 2022.

755 Hostache, R., Chini, M., Giustarini, L., Neal, J., Kavetski, D., Wood, M.,  
756 Corato, G., Pelich, R.M., Matgen, P., 2018. Near-Real-Time Assimila-  
757 tion of SAR-Derived Flood Maps for Improving Flood Forecasts. *Water*  
758 *Resources Research* 54, 5516–5535. doi:[10.1029/2017WR022205](https://doi.org/10.1029/2017WR022205).

759 Hostache, R., Martinis, S., Bauer-Marschallinger, B., Chini, M., Chow,  
760 C. Cao, S., Pelich, R., Li, Y., Böhnke, C., Knopp, L., Roth, F., Wieland,  
761 M., Wagner, W., Matgen, P., McCormick, N., Salamon, P., 2021. A first  
762 evaluation of the future CEMS systematic global flood monitoring prod-  
763 uct. [https://events.ecmwf.int/event/222/contributions/2274/  
764 attachments/1280/2347/Hydrological-WS-Hostache.pdf](https://events.ecmwf.int/event/222/contributions/2274/attachments/1280/2347/Hydrological-WS-Hostache.pdf), last access  
765 4th August 2021.

766 Janjić, T., Bormann, N., Bocquet, M., Carton, J.A., Cohn, S.E.,  
767 Dance, S.L., Losa, S.N., Nichols, N.K., Potthast, R., Waller, J.A.,  
768 Weston, P., 2018. On the representation error in data assimila-  
769 tion. Quarterly Journal of the Royal Meteorological Society 144, 1257–  
770 1278. URL: [https://rmets.onlinelibrary.wiley.com/doi/abs/10.  
771 1002/qj.3130](https://rmets.onlinelibrary.wiley.com/doi/abs/10.1002/qj.3130), doi:<https://doi.org/10.1002/qj.3130>.

772 JBA, 2021. Storm Ciara, Dennis and Jorge. [https://www.jbarisk.com/  
773 flood-services/event-response/storm-ciara-dennis-and-jorge/](https://www.jbarisk.com/flood-services/event-response/storm-ciara-dennis-and-jorge/),  
774 last access 14th September 2021.

775 Kendon, M., 2020. Storm Dennis. [https://www.metoffice.gov.  
776 uk/binaries/content/assets/metofficegovuk/pdf/weather/  
777 learn-about/uk-past-events/interesting/2020/2020\\_03\\_storm\\_  
778 dennis.pdf](https://www.metoffice.gov.uk/binaries/content/assets/metofficegovuk/pdf/weather/learn-about/uk-past-events/interesting/2020/2020_03_storm_dennis.pdf), last access 29th April 2021.

779 Leo Breiman, Jerome Friedman, C.J.S.R.O., 1984. Classification and Regres-  
780 sion Trees. Chapman and Hall/CRC.

781 Mason, D.C., Bevington, J., Dance, S.L., Revilla-Romero, B., Smith, R.,

782 Vetra-Carvalho, S., Cloke, H.L., 2021b. Improving urban flood mapping  
783 by merging synthetic aperture radar-derived flood footprints with flood  
784 hazard maps. *Water (Switzerland)* 13. doi:[10.3390/w13111577](https://doi.org/10.3390/w13111577).

785 Mason, D.C., Dance, S.L., Cloke, H.L., 2021a. Floodwater detection in urban  
786 areas using Sentinel-1 and WorldDEM data. *Journal of Applied Remote*  
787 *Sensing* 15, 1–22. doi:[10.1117/1.jrs.15.032003](https://doi.org/10.1117/1.jrs.15.032003).

788 Mason, D.C., Dance, S.L., Vetra-Carvalho, S., Cloke, H.L., 2018. Ro-  
789 bust algorithm for detecting floodwater in urban areas using syn-  
790 thetic aperture radar images. *Journal of Applied Remote Sensing* 12,  
791 1. URL: [http://centaur.reading.ac.uk/80110/8/045011{}\\_1.pdf](http://centaur.reading.ac.uk/80110/8/045011{}_1.pdf),  
792 doi:[10.1117/1.jrs.12.045011](https://doi.org/10.1117/1.jrs.12.045011).

793 Met Office, 2020. Record Breaking Rainfall. [https://www.metoffice.gov.](https://www.metoffice.gov.uk/about-us/press-office/news/weather-and-climate/302020/2020-winter-february-stats)  
794 [uk/about-us/press-office/news/weather-and-climate/302020/](https://www.metoffice.gov.uk/about-us/press-office/news/weather-and-climate/302020/2020-winter-february-stats)  
795 [2020-winter-february-stats](https://www.metoffice.gov.uk/about-us/press-office/news/weather-and-climate/302020/2020-winter-february-stats), last access 29th April 2021.

796 National River Flow Archive, 2021. NRFA. [https://nrfa.ceh.ac.uk/](https://nrfa.ceh.ac.uk/data/station/info/55002)  
797 [data/station/info/55002](https://nrfa.ceh.ac.uk/data/station/info/55002), last access 29<sup>th</sup> April 2021.

798 ndimage.zoom, 2021. Scipy. [https://docs.scipy.org/doc/scipy/](https://docs.scipy.org/doc/scipy/reference/generated/scipy.ndimage.zoom.html)  
799 [reference/generated/scipy.ndimage.zoom.html](https://docs.scipy.org/doc/scipy/reference/generated/scipy.ndimage.zoom.html), last access 21th  
800 September 2021.

801 Pappenberger, F., Frodsham, K., Beven, K., Romanowicz, R., Matgen, P.,  
802 2007. Fuzzy set approach to calibrating distributed flood inundation mod-  
803 els using remote sensing observations. *Hydrology and Earth System Sci-*  
804 *ences* 11, 739–752. doi:[10.5194/hess-11-739-2007](https://doi.org/10.5194/hess-11-739-2007).

805 Revilla-Romero, B., Shelton, K., Wood, E., Berry, R., Bevington, J., Han-  
806 kin, B., Lewis, G., Gubbin, A., Griffiths, S., Barnard, P., Pinnell, M.,  
807 Huyck, C., 2017. Flood Foresight: A near-real time flood monitoring and  
808 forecasting tool for rapid and predictive flood impact assessment, in: EGU  
809 General Assembly Conference Abstracts, p. 1230.

810 riverlevels.uk, 2020. River levels, River Wye at Hereford Bridge. [https://riverlevels.uk/herefordshire-hereford-old-wye-bridge-lvl#](https://riverlevels.uk/herefordshire-hereford-old-wye-bridge-lvl#.YIFKt31KgUE)  
811 [.YIFKt31KgUE](https://riverlevels.uk/herefordshire-hereford-old-wye-bridge-lvl#.YIFKt31KgUE), last access 29th April 2021.

813 Roberts, N.M., Lean, H.W., 2008. Scale-selective verification of rainfall ac-  
814 cumulations from high-resolution forecasts of convective events. Monthly  
815 Weather Review doi:[10.1175/2007MWR2123.1](https://doi.org/10.1175/2007MWR2123.1).

816 Schumann, G., Bates, P.D., Horritt, M.S., Matgen, P., Pappenberger, F.,  
817 2009. Progress in integration of remote sensing-derived flood extent and  
818 stage data and hydraulic models. Reviews of Geophysics doi:[10.1029/](https://doi.org/10.1029/2008RG000274)  
819 [2008RG000274](https://doi.org/10.1029/2008RG000274).

820 Sefton, C., Muchan, K., Parry, S., Matthews, B., Barker, L.J., Turner, S.,  
821 2020. The 2019 / 2020 floods in the UK : a hydrological appraisal , 1–  
822 7doi:[10.1002/wea.3993](https://doi.org/10.1002/wea.3993).

823 Skok, G., Roberts, N., 2016. Analysis of Fractions Skill Score properties for  
824 random precipitation fields and ECMWF forecasts. Quarterly Journal of  
825 the Royal Meteorological Society 142, 2599–2610. doi:[10.1002/qj.2849](https://doi.org/10.1002/qj.2849).

826 Speight, L.J., Cranston, M.D., White, C.J., Kelly, L., 2021. Operational and



827 emerging capabilities for surface water flood forecasting. Wiley Interdisci-  
828 plinary Reviews: Water 8, 1–24. doi:[10.1002/wat2.1517](https://doi.org/10.1002/wat2.1517).

829 Stein, J., Stoop, F., 2019. Neighborhood-based contingency tables including  
830 errors compensation. Monthly Weather Review 147, 329–344. doi:[10.1175/MWR-D-17-0288.1](https://doi.org/10.1175/MWR-D-17-0288.1).

832 Stephens, E., Schumann, G., Bates, P., 2014. Problems with binary pattern  
833 measures for flood model evaluation. Hydrological Processes URL: <https://doi.org/10.1002/hyp.9979>, doi:[10.1002/hyp.9979](https://doi.org/10.1002/hyp.9979).

835 Trepekli, K., Friborg, T., Balstrøm, T., Fog, B., Allotey, A., Kofie, R.,  
836 Møller-Jensen, L., 2021. UAV-LiDAR observations increase the precision  
837 of urban flood modelling in Accra by detecting critical micro-topographic  
838 features doi:[10.5194/egusphere-egu21-10457](https://doi.org/10.5194/egusphere-egu21-10457).